https://doi.org/10.5194/egusphere-2026-3542
Preprint. Discussion started: 11 August 2026

Ice–ice collisional breakup enhances secondary ice production but reduces surface hailfall in a simulated pulse hailstorm

Yi Dong[a,b,c], Shaofeng Hua[c,d], Baojun Chen[c,d] and Tuanjie Hou[c,d]

[a] *School of Atmospheric Physics, Nanjing University of Information Science and Technology (NUIST), Nanjing, China*

[b] *Chinese Academy of Meteorological Sciences (CAMS), Beijing, China*

[c] *CMA Key Laboratory of Cloud-Precipitation Physics and Weather Modification (CPML), Beijing, China*

[d] *CMA Weather Modification Centre (WMC), Beijing, China*

Corresponding authors: Shaofeng Hua, huasf@cma.gov.cn
and Baojun Chen, chenbj@cma.gov.cn

https://doi.org/10.5194/egusphere-2026-3542
Preprint. Discussion started: 11 August 2026

Abstract

Secondary ice production (SIP) can substantially modify the ice-phase structure of mixed-phase clouds, but its role in short-lived pulse hailstorms remains unclear. Here, an ice－ice collisional breakup (BR) parameterization is implemented in the NSSL two-moment scheme within Cloud Model 1 (CM1), and seven sensitivity experiments are conducted for an idealized pulse hailstorm to examine the effects of droplet shattering during freezing (DS) and BR on ice-phase evolution and surface hailfall. The results show that BR has a much stronger effect than DS on the cloud-ice structure and surface hail mass. Relative to CNTL, the experiments including BR show a marked reduction in the peak total hail mass at the surface, with the largest decrease reaching 41.94 %. BR increases the ice crystal number concentration by about two orders of magnitude between approximately 5 and 9 km, accompanied by reduced supercooled liquid water above 4 km, lower graupel mixing ratio, and weakened graupel riming growth. These changes reduce the size of potential hail embryos, weaken graupel-to-hail conversion at some heights, and limit subsequent hail growth. The decomposition of BR collision pairs shows that, during the mature hail-producing stage, collisions of ice crystals with graupel and hail become the main sources of BR fragments. Overall, BR can substantially reduce surface hail mass in this idealized pulse-hailstorm case by restructuring the ice phase and enhancing competition for supercooled liquid water.

Keywords: Hail; Numerical simulation; Pulse storm; Secondary ice production; Collisional breakup.

1. Introduction

In situ observations in many mixed-phase and deep convective clouds have shown that ice crystal number concentrations (ICNCs) often exceed ice-nucleating particle (INP) concentrations by several orders of magnitude, a discrepancy that cannot be explained by primary ice nucleation alone (Hobbs and Rangno, 1985; Cantrell and Heymsfield, 2005; Field et al., 2017; Korolev and Leisner, 2020). This discrepancy indicates the presence of secondary ice production (SIP). Various SIP mechanisms have been proposed, but their specific roles in clouds remain uncertain owing to observational limitations, making numerical models an important tool for investigating SIP processes (Korolev et al., 2017; Sullivan et al., 2017; Huang et al., 2017). Among these

https://doi.org/10.5194/egusphere-2026-3542
Preprint. Discussion started: 11 August 2026

mechanisms, the Hallett–Mossop (H–M) process has been the most widely implemented in numerical models. However, its active temperature range is limited to approximately −8 to −3 °C, and its contribution is therefore limited in the colder mixed-phase regions of deep convective clouds (Hallett and Mossop, 1974; Saunders and Hosseini, 2001). Droplet shattering during the freezing of supercooled raindrops (DS) and ice–ice collisional breakup (BR) can operate over broader temperature ranges and may therefore contribute in colder mixed-phase regions where the H–M process is inactive (Vardiman, 1978; Takahashi et al., 1995; Yano and Phillips, 2011; Phillips et al., 2017a, b; Phillips et al., 2018; Sullivan et al., 2018a; James et al., 2021). However, the relative importance of these SIP mechanisms also depends on the specific cloud microphysical conditions. In recent years, several modeling studies have incorporated SIP mechanisms into microphysics schemes. These studies indicate that in-cloud ICNCs, phase partitioning, and precipitation characteristics can change substantially due to SIP, although the dominant SIP mechanism in different cloud types remains debated (Huang et al., 2022; Qu et al., 2022, 2025; Han et al., 2024).

Previous modeling studies of SIP have considered a range of cloud types, including polar stratiform clouds, orographic mixed-phase clouds, and tropical deep convection (Sotiropoulou et al., 2020, 2021; Georgakaki et al., 2022; Huang et al., 2022), but relatively few have focused on hailstorms. Hail is a form of solid precipitation produced in severe convective storms and poses serious risks to agricultural production, property, and public safety (Prein and Holland, 2018; Allen et al., 2020). In China, hailstorms have caused substantial economic losses, with reported losses reaching hundreds of millions to several billion Chinese yuan in some periods or severe years (Tian et al., 2022). Recent studies have also shown long-term changes in hailstorm activity in China and suggested further changes under future climate warming (Zhang et al., 2025). Hail occurrence is particularly frequent in mountainous and plateau regions (Zhang et al., 2008; Li et al., 2018; Ni et al., 2020). Hail growth primarily occurs within updraft regions rich in supercooled liquid water. Additional ice crystals generated by SIP may intensify competition for this liquid water and accelerate its depletion, thereby influencing hail growth. Cloud water competition has also been identified as an important microphysical process affecting precipitation development in aerosol–cloud interactions (Zhao et al., 2024). However, how this pathway varies among different types of hailstorms remains unclear. Supercell, multicell, and pulse storms differ

https://doi.org/10.5194/egusphere-2026-3542
Preprint. Discussion started: 11 August 2026

markedly in their dynamical structures and hail growth conditions. Pulse storms are characterized by short lifetimes, weak vertical wind shear, and relatively simple dynamical backgrounds (Miller and Mote, 2017; Dong et al., 2024), making them suitable for mechanistic studies of how SIP affects hail growth. At the same time, hail growth in pulse storms is time-limited. Whether SIP-induced changes in the ice phase can be effectively transferred to hail growth and subsequently affect hailfall at the surface during this short period is a key question.

Based on a representative pulse hailstorm that occurred in Weining, Guizhou Province, China, on 27 July 2022, this study examines the effects of multiple SIP mechanisms, namely H–M, BR (based on Phillips et al. (2017a), hereafter PH17), and DS (based on Lawson et al. (2015) and Sullivan et al. (2018b)), on hail. In addition, the BR fragment source is quantitatively decomposed by collision pair to examine how the contribution of each collision pair changes during storm evolution. By combining this decomposition with microphysical conversion-rate diagnostics, this study assesses how SIP-driven restructuring of the ice phase is translated into changes in hail growth and hailfall at the surface within the short life cycle of a pulse storm. The results provide a reference for understanding the microphysical mechanisms by which SIP affects hail growth in rapidly evolving convection.

The paper is organized as follows. Sect. 2 describes the case background, model configuration, SIP parameterizations, and experimental design. Sect. 3 presents the storm evolution, microphysical responses, and contributions of BR collision pairs in each experiment. Sect. 4 summarizes the main conclusions and discusses their implications for hail growth mechanisms and SIP parameterization studies.

2. Data and Methods

2.1 Case overview and observational basis

This study is based on a pulse hailstorm that occurred in Weining, Guizhou Province, China, on 27 July 2022. The storm developed in an environment characterized by high CAPE and weak vertical wind shear and exhibited a short lifetime, rapid development, and rapid onset of hailfall, consistent with the basic features of a representative pulse storm. It therefore provides a suitable case for examining SIP mechanisms in rapidly

https://doi.org/10.5194/egusphere-2026-3542
Preprint. Discussion started: 11 August 2026

evolving convection.

The observation data used in this study are primarily from the National Hail Suppression Field Experiment conducted by the China Meteorological Administration in Guizhou Province, China, since 2021. Radar echo data were obtained from two X-band, fully solid-state, dual-polarization phased-array radars (ETWS-X02), located in Xueshan Town (104.09° E, 27.05° N) and Xinming Village (103.94° E, 26.98° N), respectively. Each radar operates at a wavelength of 3.2 cm, has 128 array antenna elements, supports horizontal and vertical polarization measurements, and has a maximum detection range of 60 km, a horizontal resolution of 30 m, and a minimum volume scan time of 30 s.

Hydrometeor classification was performed using a fuzzy logic identification framework based on polarimetric observables, including horizontal reflectivity factor (Z_H), differential reflectivity (Z_{DR}), specific differential phase (K_{DP}), and the copolar correlation coefficient (ρ_{hv}), which were used to assign weighted hydrometeor categories according to their radar signatures. Comparable fuzzy logic and X-band polarimetric hydrometeor classification methods have been described in previous studies (Park et al., 2009; Dolan and Rutledge, 2009; Al-Sakka et al., 2013; Ribaud et al., 2019).

2.2 Model configuration

Idealized numerical simulations were conducted using the three-dimensional nonhydrostatic cloud model CM1 (Cloud Model 1, version 20.3; Bryan and Fritsch, 2002), initialized with an intensive radiosonde sounding collected at 0600 UTC on 27 July 2022. The initial wind field was prescribed as zero to suppress the dynamical influence of environmental wind shear, so that SIP-related microphysical mechanisms in this type of pulse storm and their effects on hail formation and evolution could be examined more directly.

The total integration time was 180 min, with a time step of 3 s and an output interval of 60 s. The model grid contained 201 × 201 × 96 points, corresponding to a horizontal domain of 35.1 km × 35.1 km and a vertical extent of 18 km. The horizontal grid spacing was 100 m within 10.1 km of the domain center and was then uniformly

https://doi.org/10.5194/egusphere-2026-3542
Preprint. Discussion started: 11 August 2026

stretched to 400 m toward the lateral boundaries. The vertical grid spacing was 100 m below 6 km, uniformly stretched from 100 to 400 m between 6 and 10 km, and fixed at 400 m above 10 km. The simulations were performed in a large-eddy simulation (LES) configuration, and random potential temperature perturbations were introduced at the initial time.

Following Morrison et al. (2022), moist convection was initiated using perturbations in surface heat and moisture fluxes. The perturbations in surface sensible heat flux and moisture flux are denoted by H_s and H_l, respectively, and are given by

$$H_s = \begin{cases} U_s, t < 3600 \\ U_s + M_s e^{-r^2/L_H^2}, t \geq 3600 \end{cases}$$

$$H_l = \begin{cases} U_l, t < 3600 \\ U_l + M_l e^{-r^2/L_H^2}, t \geq 3600 \end{cases}, \quad (1)$$

where r is the horizontal distance from the domain center and L_H is the horizontal length scale of the enhanced fluxes. During the first 60 min of the simulation, spatially uniform background surface heat and moisture fluxes were applied over the domain, with magnitudes of $U_s = 0.03$ K m s^{-1} and $U_l = 1.2 \times 10^{-5}$ kg kg^{-1} m s^{-1}, corresponding to sensible and latent heat fluxes of approximately 35 and 35 W m^{-2}, respectively. After 60 min, Gaussian-shaped enhanced fluxes were superimposed at the domain center. In Eq. (1), $M_s = 0.3$ K m s^{-1} and $M_l = 1.2 \times 10^{-4}$ kg kg^{-1} m s^{-1}, corresponding to sensible and latent heat fluxes of approximately 350 and 350 W m^{-2}, respectively. Based on independent sensitivity tests, L_H was set to 2000 m to trigger and maintain the development of a single-cell pulse storm.

Cloud microphysical processes were represented using the NSSL two-moment bulk scheme (Mansell et al., 2010). The scheme predicts the mass mixing ratios and number concentrations of six hydrometeor categories: cloud water, rain, cloud ice, snow, graupel, and hail. It also allows the bulk densities of graupel and hail to evolve during the simulation, making it well suited for hailstorm simulations. In all experiments, the original Hallett–Mossop (H–M) process in the NSSL scheme was retained. On this basis, two DS configurations were tested, and a BR parameterization was introduced to examine the effects of different SIP mechanisms on storm development and hail characteristics.

https://doi.org/10.5194/egusphere-2026-3542
Preprint. Discussion started: 11 August 2026

2.3 SIP parameterizations

2.3.1 Droplet shattering configurations

DS represents the fragmentation of supercooled raindrops during freezing and the release of secondary ice crystals. To enable a consistent comparison among different DS schemes, the additional source term for secondary ice crystals produced by DS is written as

$$\frac{\partial N_{ice}}{\partial t}|_{DS} = N_{DS} \cdot \frac{\partial N_{freeze}}{\partial t}, \quad (2)$$

where $\frac{\partial N_{freeze}}{\partial t}$ is the number concentration tendency of freezing raindrops, and N_{DS} is the mean number of ice fragments produced by a single freezing raindrop. In addition to the CNTL experiment, two DS configurations are compared in this study. DS_LAW uses the empirical expression of Lawson et al. (2015), for which the additional source term for secondary ice crystals is

$$\frac{\partial N_{ice}}{\partial t}|_{LAW} = N_{LAW} \cdot d^4 \cdot \frac{\partial N_{freeze}}{\partial t}, \quad (3)$$

where $N_{LAW} = 2.5 \times 10^{-11}$, and d is the equivalent-volume diameter of the raindrop in μm.

DS_SUL follows the parameterization of Sullivan et al. (2018b), in which the additional source term of secondary ice crystals is expressed as

$$\frac{\partial N_{ice}}{\partial t}|_{SUL} = (p_{DS} \cdot N_{DS}) \frac{\partial N_{freeze}}{\partial t}, \quad (4)$$

where p_{DS} is the probability that a freezing raindrop shatters, given by

$$p_{DS} = \frac{p_{max}}{max\{\mathcal{N}(T_\mu, \sigma)\}} \mathcal{N}(T_\mu, \sigma), \quad (5)$$

$$\mathcal{N}(T_\mu, \sigma) = \frac{1}{\sqrt{2\pi}\sigma} exp\left[\frac{-(T-T_\mu)^2}{2\sigma^2}\right]. \quad (6)$$

This parameterization represents the shattering probability as a normal distribution function of temperature, where T_μ is the temperature at which the probability reaches

https://doi.org/10.5194/egusphere-2026-3542
Preprint. Discussion started: 11 August 2026

its maximum, set here to T_μ = 258 K; σ is the distribution width; and p_{max} is the maximum shattering probability. Following the formulation of Sullivan et al. (2018b), σ, p_{max}, and N_{DS} were set to 3 K, 20 %, and 10, respectively, to obtain a relatively pronounced DS response. The two DS configurations are included in parallel to test the sensitivity to the DS formulation and to examine the different influences of raindrop size and thermodynamic control in a pulse hailstorm.

2.3.2 Implementation of the BR parameterization

Within the original microphysical framework of the NSSL scheme, a PH17-type ice–ice collisional breakup (BR) parameterization was coupled online. The four ice-phase hydrometeor categories in NSSL, namely hail, graupel, snow, and cloud ice, were mapped to the hail, graupel, snow, and crystal types in PH17, respectively. This category mapping was kept fixed during the BR calculation, whereas particle mass, density, terminal velocity, and number concentration were diagnosed from the prognostic NSSL state.

Because the NSSL two-moment scheme predicts only the mass mixing ratio and number concentration of each hydrometeor category, it does not directly provide the particle size spectra or particle properties required by PH17. A bin-emulation approach was therefore adopted. At each physical time step and for each grid point with temperature below 273.15 K and at least one ice-phase category present, discrete size spectra were temporarily reconstructed for hail, graupel, snow, and cloud ice. Here q_x is the mass mixing ratio and c_x is the volume number concentration. The mean particle mass of category x is therefore defined as

$$\bar{m}_x = \frac{\rho_{air} q_x}{c_x}, \qquad (7)$$

where ρ_{air} is the air density. For each ice-phase category, the particle size distribution was assumed to follow a gamma distribution in diameter space. The shape parameter was set to μ = 0.5 for hail and μ = 0 for graupel, snow, and cloud ice. The slope parameter was determined using the NSSL mass–diameter relationship for each category and the diagnosed mean particle mass. Spherical mass relationships were used for hail and graupel, whereas the corresponding NSSL mass–diameter relationships were used for snow and cloud ice. This treatment allows the reconstructed size spectra

https://doi.org/10.5194/egusphere-2026-3542
Preprint. Discussion started: 11 August 2026

to remain consistent with the mass mixing ratio and number concentration predicted by the NSSL scheme.

The diagnostic diameter range for each hydrometeor category was specified according to the native physical range used for that category in the NSSL scheme, rather than being uniformly constrained to the PH17 valid diameter range during spectrum reconstruction. Each diameter range was divided into logarithmically spaced bins, and the representative diameter of each bin was taken as the geometric mean of the two bin edges. The initial number fraction in each bin was obtained by integrating the gamma distribution over the corresponding diameter interval. The bin weights were then adjusted so that the reconstructed spectrum satisfied both the total volume number concentration and total mass density constraints:

$$\sum_i n_{x,i} = c_x, \quad (8)$$

$$\sum_i n_{x,i}\, m_{x,i} = \rho_{air} q_x, \quad (9)$$

Here $n_{x,i}$ and $m_{x,i}$ are the volume number concentration and particle mass of bin i for category x, respectively. The particle mass and terminal velocity in each bin were then calculated using the corresponding NSSL mass–diameter and fall-speed relationships. The PH17 diameter range of 0.5–5 mm was not used to constrain the reconstructed spectra, but was applied only later in the calculation of empirical parameters in the fragment-number formula.

For any two bins i and j, the collision kinetic energy was calculated using the reduced-mass form:

$$K_0 = \frac{1}{2}\left(\frac{m_i m_j}{m_i + m_j}\right)(v_i - v_j)^2, \quad (10)$$

where m_i and m_j are the particle masses of the two bins, and v_i and v_j are their terminal velocities. The collision rate between any two bins i and j was estimated using a gravitational collision kernel:

$$R_{ij} = \frac{1}{4} n_i n_j \cdot \pi (D_i^{phys} + D_j^{phys})^2 |v_i - v_j| E_c, \quad (11)$$

Here, n_i and n_j are the volume number concentrations of the two bins, D_i^{phys} and D_j^{phys}

https://doi.org/10.5194/egusphere-2026-3542
Preprint. Discussion started: 11 August 2026

are the corresponding diagnosed physical diameters, E_c is the collision efficiency. For self-collisions within the same particle category, only bin combinations with $j \geqslant i$ were evaluated. A factor of 1/2 was applied for same-bin self-collisions.

For ice-phase collision pairs already represented in the native NSSL scheme, the corresponding collision efficiencies were retained. For pairs not explicitly treated in NSSL, simplified values were assigned based on the native ice-phase collision treatments: E_c = 1.0 for H–H, H–G, and G–G collisions, and E_c = 0.5 for S–S and I–I collisions. Additional sensitivity experiments using E_c = 0.5 for H–H, H–G, and G–G collisions produced qualitatively similar results, indicating that the main conclusions are not sensitive to this simplified choice. Here, H, G, S, and I denote hail, graupel, snow, and cloud ice, respectively. For example, H–G represents hail–graupel collisions, and G–I represents graupel–cloud ice collisions.

The number of fragments generated by a single collision was then calculated following PH17:

$$N_{BR} = min\{N_{max}, \alpha A(M)[1 - exp(-\left(\frac{CK_0}{\alpha A(M)}\right)^{\gamma})]\}, \quad (12)$$

where K_0 is the collision kinetic energy of the bin pair. The term $\alpha = \pi D_{calc}^2$ represents the characteristic area scale of the breaking particle, consistent with PH17. Here D_{calc} denotes the representative diameter used only in the PH17 fragment-number formula. The physical diameters diagnosed from the bin-emulation spectra were still used to calculate the collision kernel, particle mass, terminal velocity, and collision kinetic energy. For collisions between particles of the same category, the physical representative diameter was first taken as the smaller of the two particle diameters. For collisions between different categories, it was taken as the diameter of the more fragile particle. This physical representative diameter was then constrained to the PH17 valid range of 0.5–5 mm to obtain D_{calc}. The parameters A, C, γ, N_{max}, and related coefficients were specified according to the collision type, temperature, and particle characteristics in PH17. Additional implementation settings are summarized in Appendix A1.

For any two bins i and j, the number source of BR fragments was calculated as

https://doi.org/10.5194/egusphere-2026-3542
Preprint. Discussion started: 11 August 2026

$$N_{ij} = N_{BR} \times R_{ij}, \quad (13)$$

where R_{ij} is the collision rate estimated from the gravitational collision kernel. The BR calculation was performed after the NSSL process of ice multiplication from snow. The BR fragment number source was accumulated as a cloud-ice number source, and the corresponding fragment mass transfer was passed to the mass-conserving feedback step. The parent-category adjustment, mass transfer, and number concentration updates are described in Sect. 2.3.3.

To diagnose the dominant sources of BR, the calculated BR fragment number source was further accumulated separately for each ice-phase collision pair. The four ice-phase categories correspond to 10 unordered collision pairs: H–H, G–G, S–S, I–I, H–G, H–S, H–I, G–S, G–I, and S–I. In the following analysis, the "BR collision-pair contribution" refers to the percentage contribution of each collision pair to the total BR fragment number source.

2.3.3 Category adjustment and mass-conserving feedback

At the particle scale, ice–ice collisional breakup generally removes only part of the mass of the colliding particles as fragments rather than completely removing the parent particles. In the NSSL two-moment scheme, however, adding only the fragments produced by BR without adjusting the mass and number concentration of the colliding ice-phase particles may introduce artificial changes in total ice mass and mean particle size. To avoid this effect, the BR-related mass loss was accumulated diagnostically over all bin pairs for each fragile hydrometeor category x at every time step and grid point before the feedback update:

$$L_x^{BR} = \sum_{i,j} \Delta q_{x,ij}^{BR}, \quad (14)$$

where $\Delta q_{x,ij}^{BR}$ is the mass loss assigned to category x from the bin combination (i, j), and the summation is taken over all relevant collision pairs within the current time step. The mass loss actually applied was constrained by the available mass:

$$\tilde{L}_x^{BR} = min(L_x^{BR}, q_x), \quad (15)$$

where q_x is the mass mixing ratio of category x. For hail, graupel, and snow as the

https://doi.org/10.5194/egusphere-2026-3542
Preprint. Discussion started: 11 August 2026

fragile parent category, the mass mixing ratio and number concentration of the parent category were then adjusted using the same fractional reduction:

$$f_x = \frac{\tilde{L}_x^{BR}}{q_x}, \tag{16}$$

$$q_x^{new} = q_x - \tilde{L}_x^{BR}, \tag{17}$$

$$N_x^{new} = (1 - f_x)N_x. \tag{18}$$

Here, N_x denotes the number concentration of category x. For hail, graupel, and snow, the removed mass was transferred to cloud ice, and the cloud ice number concentration was increased according to the corresponding BR fragment number source. When cloud ice was the fragile category, the fragments were still assigned to cloud ice; therefore, no inter-category mass transfer was applied, and only the cloud ice number concentration was increased.

2.4 Experimental design and diagnostics

All sensitivity experiments used the same CM1 configuration and NSSL two-moment microphysics scheme described in Sect. 2.2, with only the SIP-related settings varied among the experiments. A total of seven sensitivity experiments were designed (Table 1). CNTL is the control experiment, in which only the default H–M process in the NSSL scheme is retained. All other experiments are configured relative to CNTL. DS_LAW and DS_SUL activate the two DS configurations separately. BR_PH_1 and BR_PH_2 include the BR process in addition to the default H–M process, using the 5-bin and 20-bin configurations, respectively, with DS deactivated. SIP_ALL_1 and SIP_ALL_2 combine DS_LAW with BR, also using the 5-bin and 20-bin configurations, respectively. DS_LAW is used in the combined SIP experiments because the Lawson et al. (2015) formulation is directly based on observationally inferred fragment production during freezing. Except for the SIP-related settings, the dynamical and thermodynamic conditions are identical across all experiments; therefore, differences among the experiments are primarily attributable to the SIP parameterizations.

The main diagnostics include cloud-ice structural characteristics, hail characteristics at the surface, the evolution of in-cloud microphysics, and BR sources. Unless otherwise

https://doi.org/10.5194/egusphere-2026-3542
Preprint. Discussion started: 11 August 2026

stated, all diagnostics are calculated within a horizontal analysis box centered on the domain center, extending 5.95 km from the center in both the x and y directions. "Surface" refers to the lowest model level. Vertical profiles and microphysical process rates are averaged within the main updraft region, which is further defined as grid points with $w > 2$ m s^{-1} within this horizontal analysis area. The mature-stage mean cloud-ice volume is calculated within the same horizontal analysis box and is defined as the volume of grid cells satisfying $N_i > 10^5$ kg^{-1}. In this paper, "supercooled liquid water" refers to the sum of cloud water and rainwater at temperatures below 0 °C. The BR source analysis is based on the diagnostic BR fragment number source from different collision pairs, as defined in Sect. 2.3.2. Based on the simulated evolution of hail aloft and surface hailfall in CNTL, the rapid development stage and mature hail-producing stage are defined as 90–107 min and 108–120 min, respectively.

Table 1. Overview of the numerical sensitivity experiment design. All experiments retain the default NSSL H–M process. BR_PH_1 and BR_PH_2 denote PH17-type BR calculations using 5 and 20 emulated size bins, respectively.

Experiment Name	H–M process	Droplet Shattering (DS)	Collisional Breakup (BR)	Description
CNTL	ON	OFF	OFF	Control experiment, retaining only the default NSSL H–M process
DS_LAW	ON	ON (Lawson et al., 2015)	OFF	Uses an empirical DS parameterization based on raindrop size
DS_SUL	ON	ON (Sullivan et al., 2018b)	OFF	Uses a temperature-dependent DS parameterization with a prescribed breakup probability
BR_PH_1	ON	OFF	ON (PH17; 5 bins)	BR only; bin emulation uses 5 bins
BR_PH_2	ON	OFF	ON (PH17; 20 bins)	BR only; bin emulation uses 20 bins
SIP_ALL_	ON	ON (Lawson	ON (PH17; 5	Combined experiment with

https://doi.org/10.5194/egusphere-2026-3542
Preprint. Discussion started: 11 August 2026

1		et al., 2015)	bins)	DS_LAW and BR_PH_1
SIP_ALL_2	ON	ON (Lawson et al., 2015)	ON (PH17; 20 bins)	Combined experiment with DS_LAW and BR_PH_2

https://doi.org/10.5194/egusphere-2026-3542
Preprint. Discussion started: 11 August 2026

3. Results

3.1 Observed storm structure and responses to SIP

Previous work has shown that the CNTL experiment can reasonably reproduce the convective initiation height, the 35 dBZ echo top height, the echo width, and the rapid onset of hailfall of this case (Dong et al., 2024). Figure 1 further compares the reflectivity structure and the main ice-phase particle distributions among observational retrievals, the CNTL experiment, and the SIP_ALL_2 experiment at two representative stages.

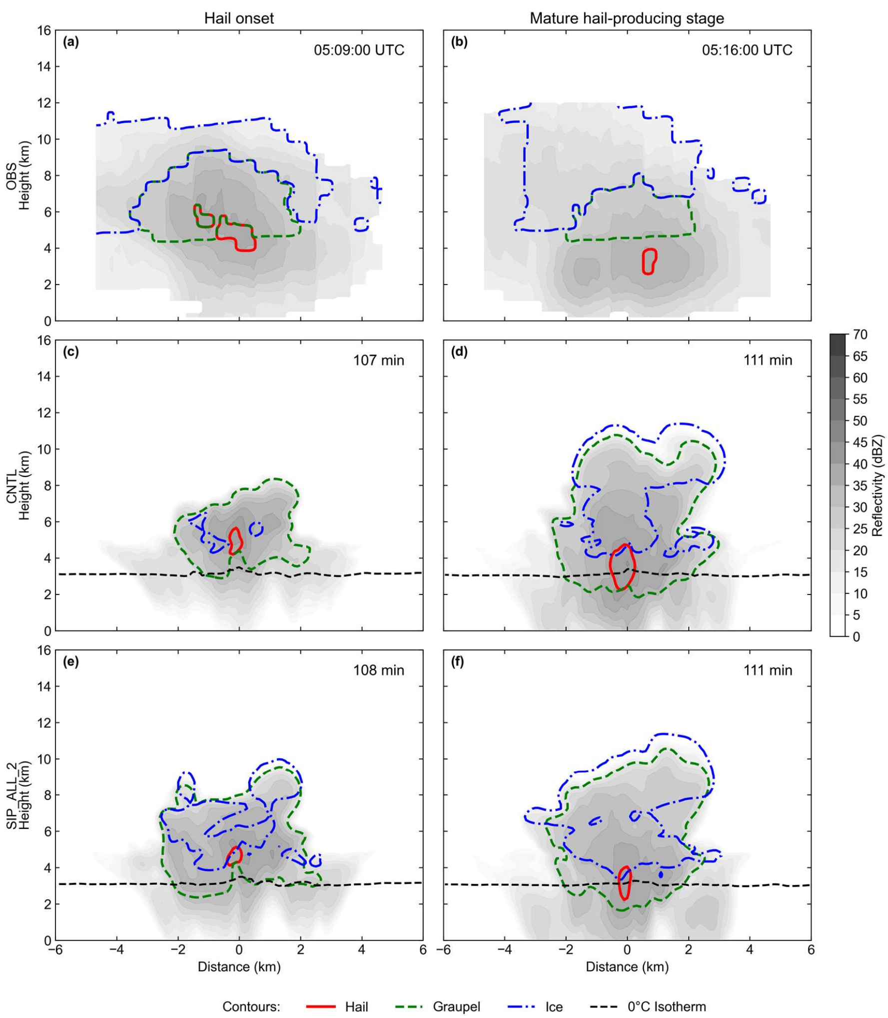

https://doi.org/10.5194/egusphere-2026-3542
Preprint. Discussion started: 11 August 2026

Figure 1. Observed and simulated storm structure at hail onset and during the mature hail-producing stage. The first column corresponds to the end of the rapid development stage, when hail first appears aloft ($q_h > 1$ g kg^{-1}), and the second column shows a representative time during the mature hail-producing stage. The grayscale shading shows reflectivity. Red, green, and blue contours denote hail, graupel, and ice crystals, respectively, and the black dashed line indicates the 0 °C isotherm.

The observational retrievals show that the pulse storm had already developed a clear vertical stratification of the ice phase during the rapid development stage (Fig. 1a). Ice crystals extended upward to approximately 11 km, graupel was concentrated between about 4.5 and 8 km, with the hail core located in the lower part of the graupel region, near 4–6 km. During the mature hail-producing stage (Fig. 1b), the hail core descended to approximately 2.5–4 km, while upper-level ice crystals remained above 10 km.

The CNTL experiment generally reproduces the main altitude ranges of graupel and hail. However, at the time when hail first appears aloft, CNTL underestimates the upper-level ice crystal region, with both the horizontal coverage and vertical extent being markedly smaller than those indicated by the observational retrievals (Fig. 1c). This bias is reduced during the mature hail-producing stage, but notable differences in the spatial distribution of ice crystals remain.

Compared with CNTL, SIP_ALL_2 produces only minor changes in the overall echo morphology but yields a more extensive mid- and upper-level ice crystal field. At the time when hail first appears aloft, the ice crystal distribution in SIP_ALL_2 is more continuous and has a broader horizontal extent than in CNTL (Fig. 1e). During the mature hail-producing stage, the upper boundary of the ice crystal field reaches around 12 km, with a broader horizontal distribution; meanwhile, the position of the hail core is also closer to that retrieved from observations (Fig. 1f). To assess whether these differences are accompanied by systematic changes in storm dynamics, cloud-ice extent, and surface hailfall, Fig. 2 compares storm-scale characteristics across the seven sensitivity experiments.

https://doi.org/10.5194/egusphere-2026-3542
Preprint. Discussion started: 11 August 2026

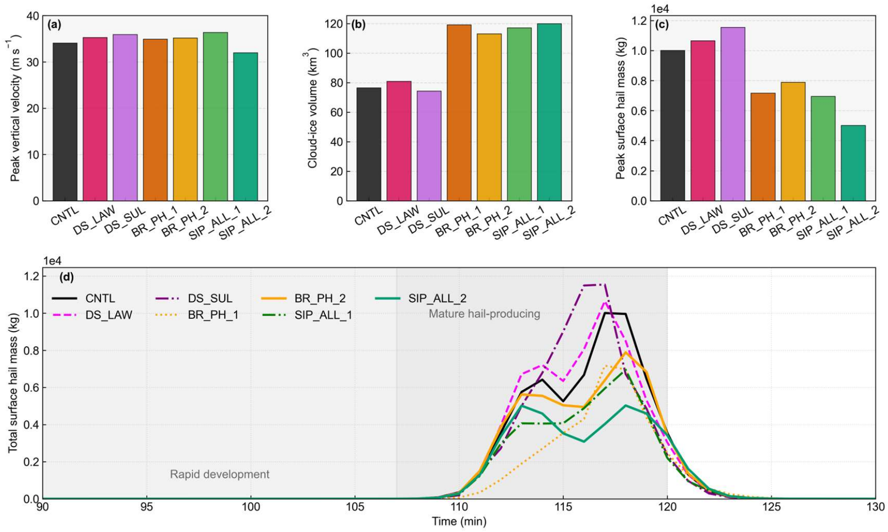

Figure 2. Storm-scale dynamical, cloud-ice, and surface hailfall responses across the sensitivity experiments. (a) Peak domain-maximum vertical velocity, (b) mature-stage mean cloud-ice volume, (c) peak total hail mass at the surface, and (d) time series of total surface hail mass. Cloud-ice volume is calculated with $N_i > 10^5$ kg^{-1} during the mature hail-producing stage. The light and dark gray shading in (d) denotes the rapid development and mature hail-producing stages, respectively.

The peak domain-maximum vertical velocity varies only weakly among the experiments, remaining roughly within 34–36.5 m s^{-1} (Fig. 2a). The two DS experiments are close to CNTL, and the BR-only and combined SIP experiments do not show a systematic enhancement. For cloud-ice volume (Fig. 2b), the DS-only experiments remain close to CNTL, whereas the BR-only and combined SIP experiments produce larger cloud-ice volumes of about 105–120 km^3. This is consistent with the broader cloud-ice region shown in the SIP_ALL_2 cross section in Fig. 1.

The peak total hail mass at the surface shows a clearer response (Fig. 2c). The two DS-only experiments produce slightly larger peak values than CNTL. In contrast, all experiments including BR markedly reduce the peak surface hail mass. Relative to CNTL, the reduction is 21.15 % in BR_PH_2, while SIP_ALL_2 produces the largest reduction among all sensitivity experiments, reaching 41.94 %. The following analysis therefore uses BR_PH_2 and SIP_ALL_2 as representative BR experiments.

Figure 2d shows the temporal evolution of total surface hail mass. In all experiments, total surface hail mass increases rapidly after about 110 min and reaches its peak shortly

https://doi.org/10.5194/egusphere-2026-3542
Preprint. Discussion started: 11 August 2026

thereafter. The peak timing is similar among the experiments, occurring between 116 and 118 min, whereas the main difference lies in the peak magnitude. The microphysical changes responsible for these differences are examined in the following section.

3.2 SIP-induced restructuring of the ice phase and liquid water competition

Figure 3 shows the mean vertical profiles of key hydrometeor properties in the five representative experiments during the mature hail-producing stage. The largest differences among the experiments occur in the ice crystal number concentration.

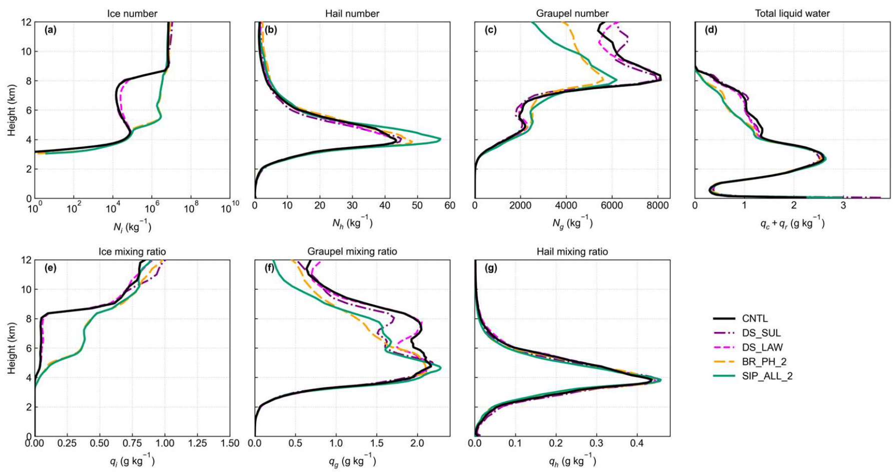

Figure 3. Mean vertical profiles of key hydrometeor properties in the analysis region during the mature hail-producing stage for representative experiments. (a) Ice crystal number concentration, (b) hail number concentration, (c) graupel number concentration, (d) total liquid water, (e) cloud ice mixing ratio, (f) graupel mixing ratio, and (g) hail mixing ratio.

Between about 5 and 9 km, N_i in BR_PH_2 and SIP_ALL_2 increases to approximately 10^6–10^7 kg^{-1}, whereas CNTL and the two DS-only experiments remain at about 10^4–10^5 kg^{-1}. At other altitudes, the differences among the experiments are smaller. This indicates that the increase in ICNC in the mid- to upper-level mixed-phase region during the mature hail-producing stage is mainly associated with BR, while the effect of DS alone is weak.

Corresponding to the increase in ICNC, the cloud ice mixing ratio in BR_PH_2 and

https://doi.org/10.5194/egusphere-2026-3542
Preprint. Discussion started: 11 August 2026

SIP_ALL_2 also increases below about 9 km, although the increase is relatively limited (Fig. 3e). The total supercooled liquid water is reduced above 4 km, especially in the mid-level mixed-phase region (Fig. 3d). The response of graupel number concentration varies with height: it increases between about 4 and 7 km but decreases above 7 km (Fig. 3c). At the same time, the graupel mixing ratio decreases overall.

For hail, the number concentration in BR_PH_2 and SIP_ALL_2 increases near 4 km, with SIP_ALL_2 showing an increase of about 30 % (Fig. 3b). The hail mixing ratio, however, does not show a clear overall change (Fig. 3g). These results indicate that BR mainly modifies the number and mass distributions of ice crystals and graupel, together with a local increase in hail number, and is accompanied by a reduction in supercooled liquid water above 4 km. To further identify the microphysical processes associated with these hydrometeor changes, Fig. 4 compares the main microphysical process rates during the mature hail-producing stage.

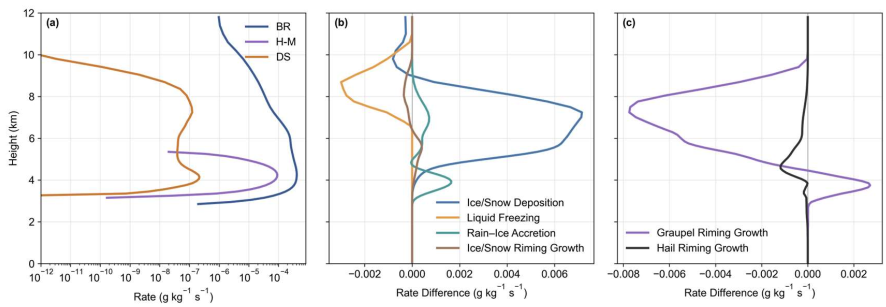

Figure 4. Mean vertical profiles of microphysical process rates in the analysis region during the mature hail-producing stage. (a) Secondary ice mass source rates associated with the three SIP processes in SIP_ALL_2. (b) Differences in the main ice-phase and liquid-water-related process rates between SIP_ALL_2 and CNTL. (c) Differences in the riming growth rates of graupel and hail between SIP_ALL_2 and CNTL. Positive values indicate larger process rates in SIP_ALL_2 than in CNTL. Detailed definitions of the process labels are provided in the Appendix.

Figure 4a shows the vertical distribution of the secondary ice mass source rates associated with the three SIP processes in SIP_ALL_2 during the mature hail-producing stage. BR contributes above approximately 3 km and reaches its maximum near 4 km, with a peak value close to 10^{-4} g kg^{-1} s^{-1}. The H–M process is mainly confined to a layer between about 3 and 5.5 km, whereas DS is generally weaker but extends to higher altitudes. Overall, BR is the dominant SIP mass source during this stage. It should be

https://doi.org/10.5194/egusphere-2026-3542
Preprint. Discussion started: 11 August 2026

noted that, although BR still has a non-negligible contribution at upper levels, its largest source rates are mainly located below 9 km, consistent with the ICNC enhancement in Fig. 3 being concentrated mainly between about 5 and 9 km.

The changes in ICNC, supercooled liquid water, and graupel mixing ratio in Fig. 3 suggest that the BR response is concentrated mainly between 4 and 9 km. To identify the processes responsible for these differences, Fig. 4b shows the differences in the main microphysical process rates between SIP_ALL_2 and CNTL. The most pronounced positive difference occurs in the depositional growth of ice crystals and snow, mainly between about 5 and 9 km, with the maximum in the mid- to upper mixed-phase region. Rain–ice accretion also increases between about 4 and 7 km. In contrast, the contribution of direct liquid freezing to ice-phase growth is reduced between about 7 and 9 km, while the riming growth of ice crystals and snow changes only weakly.

Relative to CNTL, the riming growth of graupel in SIP_ALL_2 is substantially weakened between about 5 and 9 km, especially near 7–8 km (Fig. 4c), despite a weak local enhancement near 3.5–4 km. The change in hail riming growth is smaller than that of graupel and is mainly characterized by a decrease between 4 and 7 km. These features indicate that the BR-related increase in ice crystals mainly affects liquid-water competition and graupel growth in the mid-level mixed-phase region, thereby influencing subsequent hail growth.

https://doi.org/10.5194/egusphere-2026-3542
Preprint. Discussion started: 11 August 2026

3.3 Temporal evolution of BR and its decomposition by collision pair

Figure 5a reveals the temporal evolution of the different SIP processes.

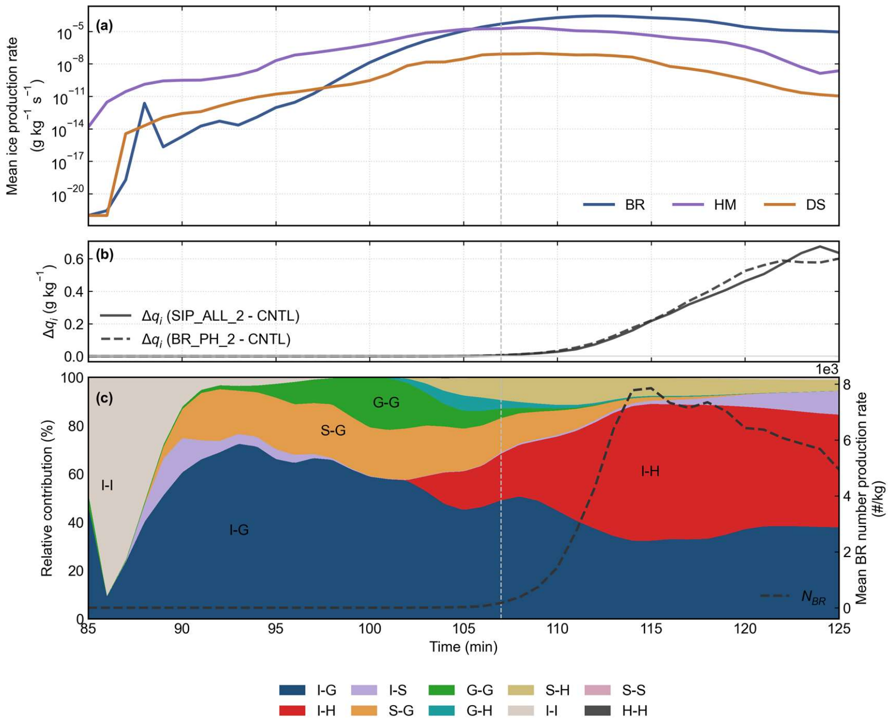

Figure 5. Temporal evolution of SIP rates, cloud ice responses, and BR collision pair contributions in SIP_ALL_2. (a) Region-mean secondary ice mass production rates from BR, H–M, and DS. (b) Region-mean cloud ice mass mixing ratio differences (Δq_i) in SIP_ALL_2 and BR_PH_2 relative to CNTL. (c) Relative contributions of the main ice-phase collision pairs to the BR fragment number source; the black dashed line denotes the region-mean BR fragment number source on the right-hand axis. The gray vertical dashed line marks 107 min, corresponding to the end of the rapid development stage.

Before 100 min, the BR mass production rate remains relatively low and is clearly smaller than that of the H–M process. BR then increases rapidly and exceeds H–M at 107 min, becoming the main SIP mass source thereafter. DS remains weak throughout the period, consistent with the vertical process-rate diagnostics in Fig. 4a.

The Δq_i values of SIP_ALL_2 and BR_PH_2 relative to CNTL both increase after 107 min (Fig. 5b). The two experiments show similar variations during 107–125 min,

https://doi.org/10.5194/egusphere-2026-3542
Preprint. Discussion started: 11 August 2026

indicating that the increase in q_i in the combined SIP experiment, relative to CNTL, is mainly attributable to BR.

To further identify the source of the BR enhancement, Fig. 5c decomposes the BR fragment number source into contributions from different ice-phase collision pairs. It should be noted that the shaded areas in Fig. 5c represent relative contributions; therefore, when the total BR number source is very small, a large percentage does not necessarily correspond to a large absolute number of fragments. Before 90 min, I–I accounts for a large fraction, but the total BR fragment number source is extremely low. As the storm develops, I–G becomes the dominant contributor during 90–103 min, accounting for more than 50 %, while S–G and G–G also make appreciable contributions. During the mature hail-producing stage, the relative contribution of I–H increases markedly, and I–H together with I–G becomes the main source of BR fragments. In contrast, I–I and the other collision types contribute less during the period of strong BR activity. These features indicate that the enhancement of BR is mainly maintained by collisions between ice crystals and larger ice-phase particles, especially graupel and hail.

https://doi.org/10.5194/egusphere-2026-3542
Preprint. Discussion started: 11 August 2026

3.4 Consequences for hail growth, hail embryos, and surface hail spectrum

The preceding results show that SIP enhancement occurs mainly during the mature hail-producing stage and is accompanied by reduced supercooled liquid water and weakened graupel riming growth in the mid- to upper-level mixed-phase region. Figure 6 further examines how these microphysical changes affect hail growth and the surface hail mass.

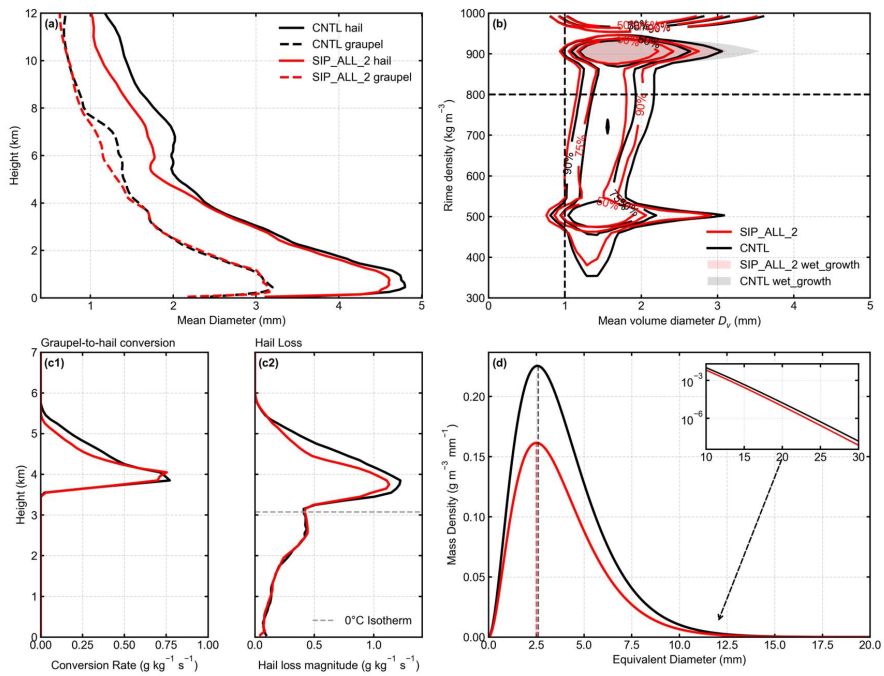

Figure 6. Region-averaged hail and graupel size responses, hail source and loss terms, and surface hail mass spectrum during the mature hail-producing stage. (a) Vertical profiles of the mean diameters of hail and graupel; (b) graupel mean volume diameter–rimed density phase space, with the dashed lines denoting the NSSL graupel-to-hail conversion thresholds of $D_v = 1$ mm and rimed density = 800 kg m^{-3}, and the shaded areas indicating the wet-growth regions; (c) hail source and loss terms, including (c1) graupel-to-hail conversion and (c2) melting plus shedding loss, with the gray dashed line denoting the mean 0 °C isotherm; and (d) surface hail mass spectrum, with the inset showing the 10–30 mm diameter range.

Figure 6a shows that the mean hail diameter in SIP_ALL_2 is generally smaller than that in CNTL above about 4 km, corresponding to the 4–8 km layer where hail growth is suppressed. The mean graupel diameter also decreases between about 4 and 8 km. In

https://doi.org/10.5194/egusphere-2026-3542
Preprint. Discussion started: 11 August 2026

the NSSL scheme, graupel can be converted to hail only when it is in the wet-growth regime, its mean volume diameter D_v exceeds 1 mm, and its rimed density exceeds 800 kg m^{-3}. In SIP_ALL_2, the graupel population shifts toward smaller diameters, and this shift is particularly evident at the large-particle end within the wet-growth region (Fig. 6b). In other words, compared with CNTL, the potential hail embryos in SIP_ALL_2 move farther away from the conditions favorable for efficient conversion to hail. This is consistent with the source-term diagnostics in Fig. 6c1: although the conversion peak near 4 km is close to that in CNTL, the graupel-to-hail conversion rate in SIP_ALL_2 is clearly reduced between about 4.5 and 5.5 km.

For hail loss, Fig. 6c2 shows that the loss caused by melting and shedding in SIP_ALL_2 is close to that in CNTL below the 0 °C level and is even smaller between about 3.5 and 5.5 km. This indicates that the reduction in surface hail mass is only weakly related to hail loss and should be mainly attributed to smaller graupel particles, weakened graupel-to-hail conversion, and limited subsequent hail growth. Could the reduced surface hail mass be caused directly by BR-induced hail mass removal? Direct mass removal from the hail category can occur only through H–H collisions, because hail is treated as the least fragile ice-phase category. However, Fig. 5c shows that the H–H contribution is negligible during the period of strong BR activity, suggesting that this direct-removal pathway is unlikely to dominate in the present implementation. Similarly, H–G and G–G collisions, which could directly remove mass from the graupel category, also contribute little during the mature hail-producing stage, while the moderate G–G contribution occurs earlier when the total BR source is still weak.

The surface hail mass spectrum is shown in Fig. 6d. Compared with CNTL, SIP_ALL_2 has a smaller peak diameter and a markedly lower mass density over the 0–10 mm diameter range, which provides the dominant contribution to the surface hail mass. Although the difference is smaller at diameters larger than 10 mm, the mass density in SIP_ALL_2 also remains lower than in CNTL in this large-particle range.

Taken together, the SIP processes, especially BR, reduce the surface hail mass through a linked set of microphysical changes. The large number of secondary ice crystals enhances competition for liquid water in the 4–8 km mixed-phase region, weakens graupel riming growth, reduces the mean size of potential hail embryos, weakens graupel-to-hail conversion over part of the layer, and suppresses the riming growth of

https://doi.org/10.5194/egusphere-2026-3542
Preprint. Discussion started: 11 August 2026

hail itself. These processes jointly lead to the reduction in surface hail mass.

4. Summary and Discussion

This study examines how different secondary ice production mechanisms affect ice-phase evolution, hail growth, and surface hailfall in a short-lived pulse hailstorm. Idealized numerical experiments were conducted using CM1 with the NSSL two-moment microphysics scheme. Two droplet-shattering configurations, an ice–ice collisional breakup parameterization, and their combined effects were tested. The main conclusions are as follows.

(1) Among the SIP mechanisms examined here, BR has a much stronger effect than DS on the simulated cloud-ice structure and surface hailfall. The experiments that include BR produce larger cloud-ice volumes during the mature hail-producing stage. However, BR does not lead to a systematic increase in the domain-maximum vertical velocity, and the peak updraft intensities remain broadly similar among the experiments. Therefore, the changes in cloud-ice volume and surface hail mass cannot be simply attributed to stronger storm-scale dynamics. The peak total hail mass at the surface is also more sensitive to BR: relative to CNTL, it decreases by 21.15 % in BR_PH_2 and by 41.94 % in SIP_ALL_2, which shows the largest reduction. These results suggest that the main effect of BR is likely to reduce surface hail mass through changes in the ice-phase structure.

(2) In the experiments including BR, the ice crystal number concentration during the mature hail-producing stage increases by about two orders of magnitude between approximately 5 and 9 km, from about 10^4–10^5 kg^{-1} in CNTL and the DS-only experiments to about 10^6–10^7 kg^{-1}. This layer corresponds to the region where supercooled liquid water decreases above 4 km and the graupel mixing ratio is reduced. Process-rate diagnostics further show that the depositional growth of ice crystals and snow is enhanced in SIP_ALL_2, and rain–ice accretion also increases, whereas graupel riming growth is markedly weakened between about 5 and 9 km. The response of hail itself is weaker: the hail mixing ratio shows little overall change, but the mean hail diameter is smaller and graupel-to-hail conversion is suppressed at some heights. Hail loss is not enhanced, indicating that the reduction in surface hail mass is mainly associated with smaller graupel particles, smaller potential hail embryos, weakened

https://doi.org/10.5194/egusphere-2026-3542
Preprint. Discussion started: 11 August 2026

graupel-to-hail conversion, and suppressed subsequent hail riming growth. The surface hail mass spectrum also shows that SIP_ALL_2 is markedly lower than CNTL over the 0–10 mm diameter range, which provides the dominant contribution to total surface hail mass.

(3) The contributions of different BR collision pairs vary distinctly during storm evolution. In the early stage, I–I collisions can account for a large relative fraction, but the BR fragment number source is very small at that time. As the storm develops, I–G becomes the dominant contributor during about 90–103 min, while S–G and G–G also make appreciable contributions. After the storm enters the mature hail-producing stage, the relative contribution of I–H increases markedly, and I–H together with I–G becomes the main source of BR fragments. In contrast, I–I and the other collision types contribute less during the mature hail-producing stage. This indicates that, in this pulse hailstorm case, the enhancement of BR is mainly maintained by collisions between ice crystals and larger ice-phase particles, especially graupel and hail. As BR produces more ice crystals, the frequency of collisions involving ice crystals may further increase, helping to maintain or enhance the BR fragment number source.

These results show that SIP can substantially regulate hail growth even in a short-lived pulse hailstorm. BR begins to increase rapidly near the end of the rapid development stage and becomes the main SIP mass source during the mature hail-producing stage. The large number of secondary ice crystals produced by BR expands the cloud-ice region and enhances competition for liquid water in the mid-level mixed-phase region. At the same time, graupel riming growth and graupel-to-hail conversion at some heights are suppressed, and subsequent hail growth is limited. As a result, the storm shows a marked reduction in surface hail mass without an evident change in dynamical intensity.

The BR response in this study is subject to uncertainties related to the PH17 parameterization and its implementation within the NSSL two-moment scheme, including the category mapping, reconstructed particle size spectra, and several simplified parameter settings. Although sensitivity experiments using different bin numbers and collision efficiencies produced qualitatively similar results, a bulk microphysics scheme cannot fully represent the diversity of ice-particle properties in real hailstorms. In addition, the simulations represent an idealized pulse hailstorm environment. Therefore, the BR response and its impacts on hail growth and surface

https://doi.org/10.5194/egusphere-2026-3542
Preprint. Discussion started: 11 August 2026

hailfall may vary among different storm types and microphysics schemes, and the associated microphysical mechanisms should be further evaluated under a broader range of storm conditions.

In addition, BR can markedly increase in-cloud ice crystal number and strengthen the competition among ice-phase particles for supercooled liquid water. This has implications for numerical simulations of hail suppression by cloud seeding. When BR is included in a model, the simulated storm may already contain many small ice crystals, resembling a relatively strong "natural seeding" state. Under such conditions, the assessment of artificial seeding effects may differ from traditional simulation studies that do not fully account for SIP processes (Atlas, 1977; Garstang et al., 2005). The presence of BR may affect the optimal timing, dosage, and location of hail-suppression seeding, as well as the criteria used to evaluate seeding effectiveness (Lu et al., 2023). However, this study also shows that the rapid increase in BR occurs mainly from the end of the rapid development stage to the mature hail-producing stage. It therefore remains unclear whether the small ice crystals produced by BR are already abundant before the key time window in which artificial seeding may be most effective. Future work should combine different storm types and seeding scenarios to systematically assess how SIP affects conclusions drawn from numerical simulations of hail suppression.

Appendix A

A1. Supplementary settings for the PH17-type BR parameterization in the NSSL bulk scheme

Sects. 2.3.2 and 2.3.3 describe the main implementation of the PH17-type BR parameterization in the NSSL scheme. Here, additional details are provided on the PH17 parameter settings and simplifying assumptions.

The empirical parameters A, C, γ and N_{max}, together with the fragment mass fraction ζ, in the PH17 formula for fragment number were assigned according to Table 1 of PH17. For particle fragility, the following order from most to least fragile is assumed:

https://doi.org/10.5194/egusphere-2026-3542
Preprint. Discussion started: 11 August 2026

cloud ice, snow, graupel, and hail.

For the rimed mass fraction Ψ in PH17, the NSSL scheme does not explicitly predict the corresponding variable required by PH17. Therefore, Ψ is fixed at 0.2, corresponding to the PH17 estimate for lightly to moderately rimed particles. Han et al. (2024) likewise prescribed the rimed fraction as a constant when implementing a PH17-type BR scheme in a bulk microphysics framework; although their default value was 0.4, additional sensitivity tests with values of 0.2, 0.3, and 0.4 produced different BR responses, although the differences among these sensitivity tests were not significant. Nevertheless, using a fixed Ψ introduces uncertainty, and its influence could be further assessed through dedicated sensitivity experiments.

Table A1. Main supplementary settings of the PH17-type BR parameterization used in this study.

Item	Setting in this study	Description
PH17 empirical parameters	A, C, γ, N_{max}, and ζ are taken from Table 1 of PH17	Original PH17 parameter values are used.
Category mapping	I, S, G, and H correspond to the PH17 categories of crystal, snow, graupel, and hail, respectively.	Consistent with the four ice-phase categories in the NSSL scheme.
Representative diameter D	Limited to 0.5–5 mm	Values outside this range are truncated to the nearest bound.
Ice/snow habit	Dendritic between −12 and −17 °C; spatial planar at other subzero temperatures	Following PH17 guidance for models that do not explicitly predict ice habit.
Rimed fraction Ψ	Fixed at $\Psi = 0.2$	Represents lightly to moderately rimed particles.

A2. Microphysical process labels in Fig. 4

Table A2 lists the process labels used in the microphysical conversion-rate diagnostics

https://doi.org/10.5194/egusphere-2026-3542
Preprint. Discussion started: 11 August 2026

in Fig. 4 and their physical meanings.

Table A2. Meanings of the microphysical process labels used in Fig. 4.

Label in Fig. 4	Physical meaning
Ice/Snow Deposition	Depositional growth of cloud ice and snow by water vapor deposition
Liquid Freezing	Freezing of liquid hydrometeors
Rain–Ice Accretion	Freezing of raindrops collected by ice particles
Ice/Snow Growth	Growth of cloud ice and snow by riming supercooled liquid water
Graupel Riming Growth	Growth of graupel by riming supercooled liquid water
Hail Riming Growth	Growth of hail by riming supercooled liquid water

Code and data availability.

The data and code used in this study are available from Zenodo at https://doi.org/10.5281/zenodo.20556202 (Dong et al., 2026). The archive contains the CM1 input sounding and namelist files for all sensitivity experiments, the modified CM1/NSSL-BR source-code files and patch, the processed figure-source data and selected NetCDF slices for Figs. 1–6, metadata files, and the Python plotting scripts. Complete raw CM1 history files are not included because of their large size, but the provided files are sufficient to reproduce the manuscript figures and rerun the simulations.

Author contribution.

YD conceptualized the study, curated the data, developed the methodology, implemented the model modifications, performed the simulations and analysis, and wrote the original manuscript draft. SH contributed to the investigation, project administration, interpretation of the results, and manuscript review and editing. BC contributed to the investigation, project administration, interpretation of the results, and manuscript review and editing. TH contributed to manuscript review and editing. All authors discussed the results and contributed to the final version of the manuscript.

https://doi.org/10.5194/egusphere-2026-3542
Preprint. Discussion started: 11 August 2026

Competing interests.

The authors declare that they have no conflict of interest.

Financial support.

This work was supported by the National Natural Science Foundation of China (grant no. 42405091), the CMA Key Innovation Team (grant no. CMA2022ZD10), and the S&T Development Fund of CAMS (grant no. 2025KJ022).

https://doi.org/10.5194/egusphere-2026-3542
Preprint. Discussion started: 11 August 2026

References

Allen, J. T., Giammanco, I. M., Kumjian, M. R., Punge, H. J., Zhang, Q., Groenemeijer, P., Kunz, M., and Ortega, K.: Understanding Hail in the Earth System, Reviews of Geophysics, 58, e2019RG000665, https://doi.org/10.1029/2019RG000665, 2020.

Al-Sakka, H., Boumahmoud, A.-A., Fradon, B., Frasier, S. J., and Tabary, P.: A New Fuzzy Logic Hydrometeor Classification Scheme Applied to the French X-, C-, and S-Band Polarimetric Radars, Journal of Applied Meteorology and Climatology, 52, 2328 – 2344, https://doi.org/10.1175/JAMC-D-12-0236.1, 2013.

Atlas, D.: The Paradox of Hail Suppression: Under different circumstances, cloud seeding may result in either increased or decreased hail., Science, 195, 139 – 145, https://doi.org/10.1126/science.195.4274.139, 1977.

Bryan, G. H. and Fritsch, J. M.: A Benchmark Simulation for Moist Nonhydrostatic Numerical Models, Mon. Wea. Rev., 130, 2917 – 2928, https://doi.org/10.1175/1520-0493(2002)130<2917:ABSFMN>2.0.CO;2, 2002.

Cantrell, W. and Heymsfield, A.: Production of Ice in Tropospheric Clouds: A Review, Bull. Amer. Meteor. Soc., 86, 795 – 808, https://doi.org/10.1175/BAMS-86-6-795, 2005.

Dolan, B. and Rutledge, S. A.: A Theory-Based Hydrometeor Identification Algorithm for X-Band Polarimetric Radars, Journal of Atmospheric and Oceanic Technology, 26, 2071 – 2088, https://doi.org/10.1175/2009JTECHA1208.1, 2009.

Dong, Y., Hua, S., Chen, B., Wang, H., and Hou, T.: Numerical simulation of a pulse hailstorm in the plateau region in southwestern China, Atmospheric Research, 299, 107218, https://doi.org/10.1016/j.atmosres.2023.107218, 2024.

Dong, Y., Hua, S., Chen, B., and Hou, T.: Data and code for “Ice–ice collisional breakup enhances secondary ice production but reduces surface hailfall in a simulated pulse hailstorm”, Zenodo [data set and code], https://doi.org/10.5281/zenodo.20556202, 2026.

Field, P. R., Lawson, R. P., Brown, P. R. A., Lloyd, G., Westbrook, C., Moisseev, D., Miltenberger, A., Nenes, A., Blyth, A., Choularton, T., Connolly, P., Buehl, J., Crosier, J., Cui, Z., Dearden, C., DeMott, P., Flossmann, A., Heymsfield, A., Huang, Y., Kalesse, H., Kanji, Z. A., Korolev, A., Kirchgaessner, A., Lasher-Trapp, S., Leisner, T., McFarquhar, G., Phillips, V., Stith, J., and Sullivan, S.: Chapter 7. Secondary Ice Production - current state of the science and recommendations for the future, Meteorological Monographs, AMSMONOGRAPHS-D-16-0014.1, https://doi.org/10.1175/AMSMONOGRAPHS-D-16-0014.1, 2017.

Garstang, M., Bruintjes, R., Serafin, R., Orville, H., Boe, B., Cotton, W., and Warburton, J.: Weather Modification: Finding Common Ground, Bull. Amer. Meteor. Soc., 86, 647 – 656, https://doi.org/10.1175/BAMS-86-5-647, 2005.

Georgakaki, P., Sotiropoulou, G., Vignon, É., Billault-Roux, A.-C., Berne, A., and Nenes, A.: Secondary ice production processes in wintertime alpine mixed-phase clouds, Atmos. Chem. Phys., 22, 1965 – 1988, https://doi.org/10.5194/acp-22-1965-2022, 2022.

Hallett, J. and Mossop, S. C.: Production of secondary ice particles during the riming process, Nature, 249, 26 – 28, https://doi.org/10.1038/249026a0, 1974.

Han, C., Hoose, C., and Dürlich, V.: Secondary Ice Production in Simulated Deep Convective Clouds: A Sensitivity Study, Journal of the Atmospheric Sciences, 81, 903 – 921, https://doi.org/10.1175/JAS-D-23-0156.1, 2024.

Hobbs, P. V. and Rangno, A. L.: Ice Particle Concentrations in Clouds, J. Atmos. Sci., 42, 2523 – 2549, https://doi.org/10.1175/1520-0469(1985)042<2523:IPCIC>2.0.CO;2, 1985.

https://doi.org/10.5194/egusphere-2026-3542
Preprint. Discussion started: 11 August 2026

Huang, Y., Blyth, A. M., Brown, P. R. A., Choularton, T. W., and Cui, Z.: Factors controlling secondary ice production in cumulus clouds, Quart J Royal Meteoro Soc, 143, 1021–1031, https://doi.org/10.1002/qj.2987, 2017.

Huang, Y., Wu, W., McFarquhar, G. M., Xue, M., Morrison, H., Milbrandt, J., Korolev, A. V., Hu, Y., Qu, Z., Wolde, M., Nguyen, C., Schwarzenboeck, A., and Heckman, I.: Microphysical processes producing high ice water contents (HIWCs) in tropical convective clouds during the HAIC-HIWC field campaign: dominant role of secondary ice production, Atmos. Chem. Phys., 22, 2365–2384, https://doi.org/10.5194/acp-22-2365-2022, 2022.

James, R. L., Phillips, V. T. J., and Connolly, P. J.: Secondary ice production during the break-up of freezing water drops on impact with ice particles, Atmos. Chem. Phys., 21, 18519–18530, https://doi.org/10.5194/acp-21-18519-2021, 2021.

Korolev, A. and Leisner, T.: Review of experimental studies of secondary ice production, Atmos. Chem. Phys., 20, 11767–11797, https://doi.org/10.5194/acp-20-11767-2020, 2020.

Korolev, A., McFarquhar, G., Field, P. R., Franklin, C., Lawson, P., Wang, Z., Williams, E., Abel, S. J., Axisa, D., Borrmann, S., Crosier, J., Fugal, J., Krämer, M., Lohmann, U., Schlenczek, O., Schnaiter, M., and Wendisch, M.: Mixed-Phase Clouds: Progress and Challenges, Meteorological Monographs, 58, 5.1-5.50, https://doi.org/10.1175/AMSMONOGRAPHS-D-17-0001.1, 2017.

Lawson, R. P., Woods, S., and Morrison, H.: The Microphysics of Ice and Precipitation Development in Tropical Cumulus Clouds, Journal of the Atmospheric Sciences, 72, 2429–2445, https://doi.org/10.1175/JAS-D-14-0274.1, 2015.

Li, X., Zhang, Q., Zou, T., Lin, J., Kong, H., and Ren, Z.: Climatology of Hail Frequency and Size in China, 1980–2015, Journal of Applied Meteorology and Climatology, 57, 875–887, https://doi.org/10.1175/JAMC-D-17-0208.1, 2018.

Lu, Y., Zhou, Y., Zou, S., Yang, Z., and Zeng, Y.: The Macro- and Microphysical Response Characteristics of the Multicell Hailstorm Hail-Suppression Operation: Case Study, Journal of Applied Meteorology and Climatology, 62, 1243–1262, https://doi.org/10.1175/JAMC-D-22-0129.1, 2023.

Mansell, E. R., Ziegler, C. L., and Bruning, E. C.: Simulated Electrification of a Small Thunderstorm with Two-Moment Bulk Microphysics, Journal of the Atmospheric Sciences, 67, 171–194, https://doi.org/10.1175/2009JAS2965.1, 2010.

Miller, P. W. and Mote, T. L.: Standardizing the Definition of a “Pulse” Thunderstorm, Bulletin of the American Meteorological Society, 98, 905–913, https://doi.org/10.1175/BAMS-D-16-0064.1, 2017.

Morrison, H., Peters, J. M., Chandrakar, K. K., and Sherwood, S. C.: Influences of Environmental Relative Humidity and Horizontal Scale of Subcloud Ascent on Deep Convective Initiation, Journal of the Atmospheric Sciences, 79, 337–359, https://doi.org/10.1175/JAS-D-21-0056.1, 2022.

Ni, X., Muehlbauer, A., Allen, J. T., Zhang, Q., and Fan, J.: A Climatology and Extreme Value Analysis of Large Hail in China, Monthly Weather Review, 148, 1431–1447, https://doi.org/10.1175/MWR-D-19-0276.1, 2020.

Park, H. S., Ryzhkov, A. V., Zrnić, D. S., and Kim, K.-E.: The Hydrometeor Classification Algorithm for the Polarimetric WSR-88D: Description and Application to an MCS, Weather and Forecasting, 24, 730–748, https://doi.org/10.1175/2008WAF2222205.1, 2009.

Phillips, V. T. J., Yano, J.-I., and Khain, A.: Ice Multiplication by Breakup in Ice–Ice Collisions.

https://doi.org/10.5194/egusphere-2026-3542
Preprint. Discussion started: 11 August 2026

Part I: Theoretical Formulation, Journal of the Atmospheric Sciences, 74, 1705–1719, https://doi.org/10.1175/JAS-D-16-0224.1, 2017a.

Phillips, V. T. J., Yano, J.-I., Formenton, M., Ilotoviz, E., Kanawade, V., Kudzotsa, I., Sun, J., Bansemer, A., Detwiler, A. G., Khain, A., and Tessendorf, S. A.: Ice Multiplication by Breakup in Ice–Ice Collisions. Part II: Numerical Simulations, Journal of the Atmospheric Sciences, 74, 2789–2811, https://doi.org/10.1175/JAS-D-16-0223.1, 2017b.

Phillips, V. T. J., Patade, S., Gutierrez, J., and Bansemer, A.: Secondary Ice Production by Fragmentation of Freezing Drops: Formulation and Theory, Journal of the Atmospheric Sciences, 75, 3031–3070, https://doi.org/10.1175/JAS-D-17-0190.1, 2018.

Prein, A. F. and Holland, G. J.: Global estimates of damaging hail hazard, Weather and Climate Extremes, 22, 10–23, https://doi.org/10.1016/j.wace.2018.10.004, 2018.

Qu, Z., Korolev, A., Milbrandt, J. A., Heckman, I., Huang, Y., McFarquhar, G. M., Morrison, H., Wolde, M., and Nguyen, C.: The impacts of secondary ice production on microphysics and dynamics in tropical convection, Atmos. Chem. Phys., 22, 12287–12310, https://doi.org/10.5194/acp-22-12287-2022, 2022.

Qu, Z., Korolev, A., Milbrandt, J. A., Heckman, I., Cholette, M., Nguyen, C., and Wolde, M.: The impacts of secondary ice production on the microphysics and dynamics of mid-latitude cold season convection, Atmos. Chem. Phys., 25, 17845–17868, https://doi.org/10.5194/acp-25-17845-2025, 2025.

Ribaud, J.-F., Machado, L. A. T., and Biscaro, T.: X-band dual-polarization radar-based hydrometeor classification for Brazilian tropical precipitation systems, Atmos. Meas. Tech., 12, 811–837, https://doi.org/10.5194/amt-12-811-2019, 2019.

Saunders, C. P. R. and Hosseini, A. S.: A laboratory study of the effect of velocity on Hallett–Mossop ice crystal multiplication, Atmospheric Research, 59–60, 3–14, https://doi.org/10.1016/S0169-8095(01)00106-5, 2001.

Sotiropoulou, G., Sullivan, S., Savre, J., Lloyd, G., Lachlan-Cope, T., Ekman, A. M. L., and Nenes, A.: The impact of secondary ice production on Arctic stratocumulus, Atmos. Chem. Phys., 20, 1301–1316, https://doi.org/10.5194/acp-20-1301-2020, 2020.

Sotiropoulou, G., Vignon, É., Young, G., Morrison, H., O'Shea, S. J., Lachlan-Cope, T., Berne, A., and Nenes, A.: Secondary ice production in summer clouds over the Antarctic coast: an underappreciated process in atmospheric models, Atmos. Chem. Phys., 21, 755–771, https://doi.org/10.5194/acp-21-755-2021, 2021.

Sullivan, S. C., Hoose, C., and Nenes, A.: Investigating the contribution of secondary ice production to in-cloud ice crystal numbers, JGR Atmospheres, 122, 9391–9412, https://doi.org/10.1002/2017JD026546, 2017.

Sullivan, S. C., Hoose, C., Kiselev, A., Leisner, T., and Nenes, A.: Initiation of secondary ice production in clouds, Atmos. Chem. Phys., 18, 1593–1610, https://doi.org/10.5194/acp-18-1593-2018, 2018a.

Sullivan, S. C., Barthlott, C., Crosier, J., Zhukov, I., Nenes, A., and Hoose, C.: The effect of secondary ice production parameterization on the simulation of a cold frontal rainband, Atmos. Chem. Phys., 18, 16461–16480, https://doi.org/10.5194/acp-18-16461-2018, 2018b.

Takahashi, T., Nagao, Y., and Kushiyama, Y.: Possible High Ice Particle Production during Graupel–Graupel Collisions, J. Atmos. Sci., 52, 4523–4527, https://doi.org/10.1175/1520-0469(1995)052<4523:PHIPPD>2.0.CO;2, 1995.

Tian, Y., Yao, W., Sun, Y., Wang, Y., Liu, X., Jiang, T., Zhang, L., Meng, L., Wang, L., Sun, X.,

https://doi.org/10.5194/egusphere-2026-3542
Preprint. Discussion started: 11 August 2026

and Wang, H.: A method for improving the performance of the 2σ lightning jump algorithm for nowcasting hail, Atmospheric Research, 280, 106404, https://doi.org/10.1016/j.atmosres.2022.106404, 2022.

Vardiman, L.: The Generation of Secondary Ice Particles in Clouds by Crystal–Crystal Collision, J. Atmos. Sci., 35, 2168–2180, https://doi.org/10.1175/1520-0469(1978)035<2168:TGOSIP>2.0.CO;2, 1978.

Yano, J.-I. and Phillips, V. T. J.: Ice–Ice Collisions: An Ice Multiplication Process in Atmospheric Clouds, Journal of the Atmospheric Sciences, 68, 322–333, https://doi.org/10.1175/2010JAS3607.1, 2011.

Zhang, C., Zhang, Q., and Wang, Y.: Climatology of Hail in China: 1961–2005, Journal of Applied Meteorology and Climatology, 47, 795–804, https://doi.org/10.1175/2007JAMC1603.1, 2008.

Zhang, Q., Li, R., Li, W., Li, X., Ng, C.-P., Zhang, S., and Zhao, C.: Climate impacts and future trends of hailstorms in China based on millennial records, Nat. Commun., 16, 8000, https://doi.org/10.1038/s41467-025-63028-7, 2025.

Zhao, C., Sun, Y., Yang, J., Li, J., Zhou, Y., Yang, Y., Fan, H., and Zhao, X.: Observational evidence and mechanisms of aerosol effects on precipitation, Sci. Bull., 69, 1569–1580, https://doi.org/10.1016/j.scib.2024.03.014, 2024.